

Uncovering the system vulnerability and criticality of human brain under evolving neuropathological events in Alzheimer's disease

Jingwen Zhang¹, Qing Liu², Haorui Zhang², Michelle Dai¹, Qianqian Song³, Defu Yang⁴, Guorong Wu^{4,5}, Minghan Chen¹, and Alzheimer's Disease Neuroimaging Initiative (ANDI)

Author affiliations:

¹ Department of Computer Science, Wake Forest University, Winston-Salem, NC 27109, USA

² Department of Mathematics and Statistics, Wake Forest University, Winston-Salem, NC 27109, USA

³ Department of Cancer Biology, Wake Forest School of Medicine, Winston Salem, NC 27101, USA

⁴ Department of Psychiatry, University of North Carolina at Chapel Hill, Chapel Hill, NC 27599, USA

⁵ Department of Computer Science, University of North Carolina at Chapel Hill, Chapel Hill, NC 27599, USA

Corresponding author and lead contact: Minghan Chen

Full address: 242 Manchester Hall, Department of Computer Science, Wake Forest University, 27109

E-mail: chenm@wfu.edu

Abstract

Despite the striking efforts in investigating neurobiological factors behind the acquisition of beta-amyloid (A), protein tau (T), and neurodegeneration ([N]) biomarkers, the mechanistic pathways of how AT[N] biomarkers spreading throughout the brain remain elusive. In this work, we characterized the interaction of AT[N] biomarkers and their propagation across brain networks using a novel bistable reaction-diffusion model, which allows us to establish a new systems biology underpinning of Alzheimer's disease (AD) progression. We applied our model to a large-scale longitudinal neuroimages from the ADNI database and studied the systematic vulnerability and criticality of brains. Our major findings include (i) tau is a stronger indicator of regional risk compared to amyloid, (ii) the progression of amyloid and tau follow the Braak-like pattern across the brain, (iii) temporal lobe exhibits higher vulnerability to AD-related pathologies, and (iv) proposed critical brain regions outperforms hub nodes in transmitting disease factors across brain.

Keywords: Alzheimer's disease, AT[N] biomarkers, brain network, reaction-diffusion model, vulnerable and critical regions

1. Introduction

Alzheimer's disease (AD), a progressive neurological disorder, is documented by post-mortem examination or by biomarkers *in vivo*, according to the National Institute of Aging and Alzheimer's Association (NIA-AA)¹. The biomarker framework proposed by NIA-AA for clinical diagnosis includes: (i) extracellular plaques consisting of beta-amyloid ($A\beta$, referred to as A biomarker)²⁻⁴; (ii) intracellular neurofibrillary tangles (NFT) that are the intraneuronal aggregation of hyperphosphorylated tau protein (referred to as T biomarker)^{5,6}; and (iii) neurodegeneration (referred to as [N] biomarker) that is characterized by neuronal loss and exhibits metabolic, structural, and functional deficiency⁷.

From the mainstream viewpoint, beta-amyloid triggers a series of downstream pathological responses, including inflammatory responses, hyperphosphorylation of tau protein, and AD progression^{8,9}. Tau protein helps to stabilize microtubules, but when hyperphosphorylated, it disassembles from axons, aggregates into neurofibrillary tangles, blocks neuron-to-neuron transportation, and consequently leads to the loss of synaptic functions and neurons^{5,6}. The toxicities of pathological amyloid and tau lead to malfunctioning neurons, which further induces neurodegeneration, the molecular manifestation of brain atrophy or malfunctioning neurons in both normal aging brains and neurodegenerative diseases including Alzheimer's disease^{5,7,10}.

Recently, both clinical and computational findings support the trending mechanistic hypothesis that the spread of AT[N] biomarkers exhibits a specific temporal and diffusive pattern.¹¹⁻¹³ Increasing attention has been paid to the spatial and temporal correlation between tau depositions and neuron losses. Some researchers favor the tau hypothesis^{5,6,14} over the amyloid hypothesis^{15,16} as amyloid is poorly matched to the spatial distribution and temporal evolution of neuron loss. Yet, the abnormal transformation of tau is proven to be mediated by beta-amyloid^{17,18}. Moreover, several studies emphasize the necessity of both beta-amyloid and tau in AD development by showing that tau does not lead to AD in the absence of amyloid accumulation^{9,10}. In this context, it is crucial to study the interaction between amyloid and tau and their dynamic impact on the pathophysiological mechanism of AD.

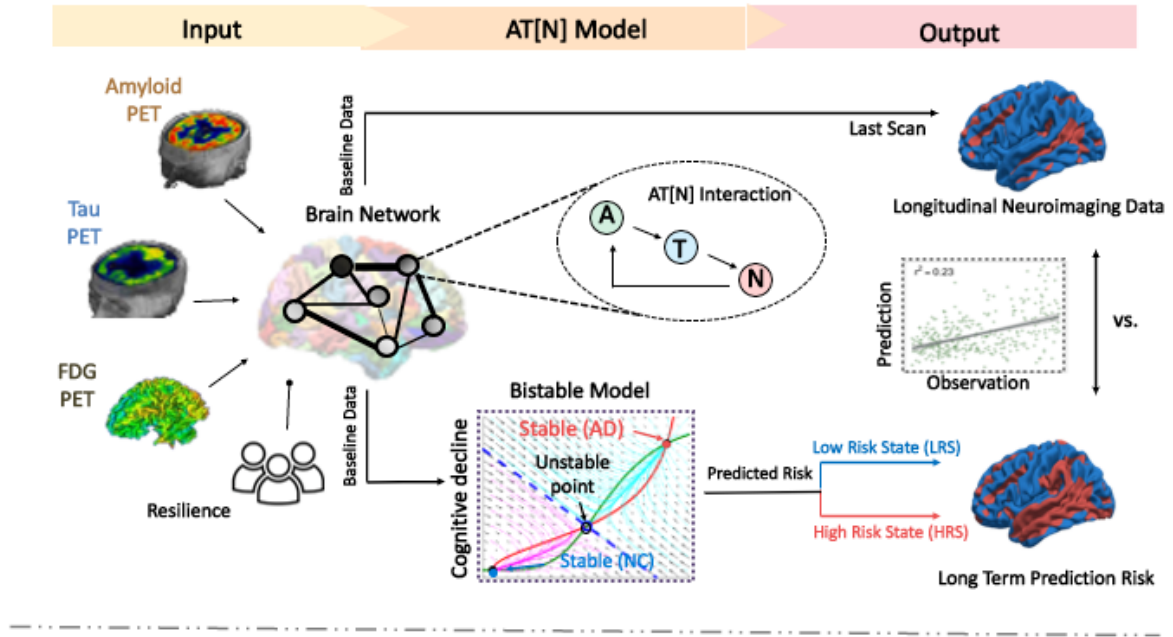
The recent advance of neuroimaging techniques offers a window to measure the pathological burden and structural atrophy *in vivo* along with the progression of AD. Currently, most neuroimaging studies utilize association-based approaches to understand the neurobiology risk factors behind AD progression, which only addresses "mechanisms" by proxy. The lack of a system-level understanding oftentimes makes current findings distinct from essential physiopathological mechanisms. In this regard, the pioneering network-diffusion model^{11,19} was used to predict longitudinal atrophy patterns from MRI (Magnetic Resonance Imaging) images. The recent epidemic spread model^{18,20} investigated the spread of amyloid and tau on structural and functional networks. However, those models only describe the diffusion process of disease factors while ignoring the fundamental interactive pathways between AT[N] biomarkers. Although tremendous efforts have been made to model complex biological systems, most AD-related systems biology approaches are limited to studying a single

pathological pathway or a small part of the brain, lacking the whole-brain insight gained from the large-scale longitudinal neuroimaging data^{21,22}.

This work aims to understand the pathophysiological mechanism of AD by probing into the spatiotemporal dynamics of AT[N] biomarkers on the whole-brain scale. We conceptualize that AD-related biomarkers not only interactively contribute to the neurodegenerative process at each brain region but also influence the connected regions in a prion-like manner. To this end, we deploy a network-guided bistable model to characterize the AT[N] cascade interactions and diffusion patterns (Fig. 1B). The longitudinal neuroimaging data is used as the benchmark to evaluate the predicted evolutionary trajectory, including (i) regional AT[N] biomarker concentration levels extracted from PET scans and (ii) structural brain networks constructed from T1-weighted MRI and diffusion-weighted imaging (DWI) scans (see the *input* in Fig. 1A). We also include the cognitive reserve proxy²³ to model the resistance to neuropathology burden. The model converges to two stable steady states (shown in the green dash box of Fig. 1A): the low-energy cognitive normal state (low-risk state, LRS) and the high-energy AD state (high-risk state, HRS), which lays the cornerstone for prediction risk, a key indicator of AD likelihood.

Model outcomes present an overall strong linear correlation between prognostic and diagnostic results (see the *output* in Fig. 1A) and capture the Braak-like spread pattern of AT[N] biomarkers in AD development. Furthermore, based on system behaviors manifested in the reaction-diffusion model, we are able to identify brain regions that suffer great vulnerability to the abnormal AT[N] attacks, as well as to nominate a collection of nodes that reveal critical importance to pathological progression across the brain under complex neuropathological events. Those discoveries set the stage for precision medicine and disease-modifying treatment.

A. Methodological Process



B. Bistable Reaction-Diffusion Model

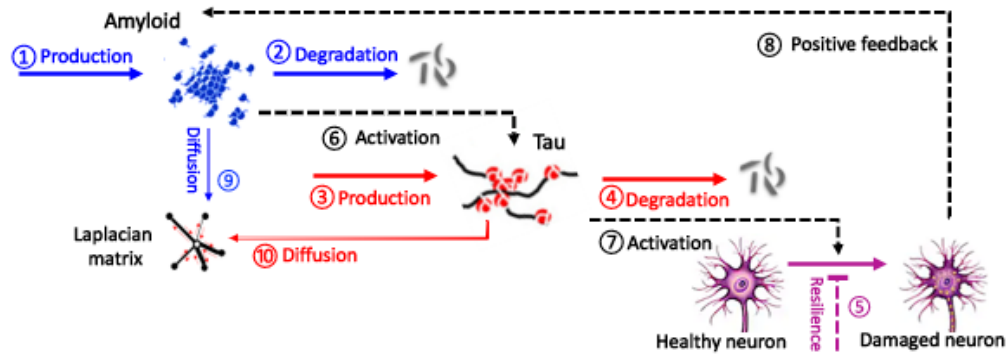


Figure 1. Overview. (A) Methodological process. **Input:** Amyloid-, Tau-, FDG-PET, DWI scans, and cognitive reserve proxy are processed and used as indicators of regional AT[N] biomarker level, network connectivity, and neuropathological resistance, respectively. **AT[N] Model:** our reaction-diffusion model is built on the AT[N] cascade mechanism and characterizes bistable states (low-, high-risk states) of the system. **Output:** model outputs long-term prediction risk, represented as a surface rendering of regional low/high risks. A moderate positive correlation is observed ($r^2 = 0.23$) between the prognostic (based on baseline scans) and diagnostic results (based on last scans). In particular, the last scans of regional neurodegeneration levels of each subject are classified into low/high states using the optimal cutoff value found from receiver operating characteristic analysis by maximizing the sum of sensitivity and specificity. (B) Bistable reaction-diffusion model. The backbone of our proposed model is built on the interactive pathways and neuronal prion-like propagation hypothesis of AT[N] biomarkers: beta-amyloid activates the hyperphosphorylation of tau protein, and the abnormal tau triggers neurodegeneration which then leads to AD; both amyloid and tau spread across the brain network in a prion-like manner. See *Materials and methods* section for detailed descriptions of mechanistic pathways.

2. Materials and methods

2.1 Participants

All data used in this study were leveraged from Alzheimer’s Disease Neuroimaging Initiative (ADNI) database. In total, 1616 subjects from ADNI passed our quality control after image processing and parcellation. Among them, 320 participants were selected to train the model based on three criteria: (i) have AV45 Amyloid-PET, AV1451 Tau-PET, FDG-PET, T1-weighted MRI, and DWI scans; (ii) have at least one follow-up PET scan of A, T, or [N]; (iii) have a clinical diagnostic label (CN, SMC, EMCI, LMCI, and AD) for each PET scan. Note that FDG data (a measure of tissue glucose metabolism) is used as a reversed indicator of neurodegeneration. Region-to-region connectivity strength, measured by the count of white matter fibers, is also utilized to characterize brain network diffusion.

2.2 Data processing

MRI data. Using the software of FreeSurfer²⁴, all MRI data were processed through four steps: 1) Skull stripping; 2) tissue segmentation into white matter, gray matter, and cerebrospinal fluid; 3) cortical surface reconstruction based on tissue segmentation map; and 4) cortical surface parcellation into 148 regions of Destrieux atlas²⁵ using deformable image registration.

Brain network construction. First, we aligned the DWI images to the corresponding T1-weighted MR image for each subject. We then followed the parcellation of cortical surface and applied the surface seed-based probabilistic fiber tractography in FreeSurfer, generating a 148×148 connectivity matrix. The weight of the anatomical connectivity of pair-wise regions is measured by the number of fibers connecting two regions.

PET data. Each PET scan (Amyloid-PET, Tau-PET, FDG-PET) was aligned with their own subject’s T1-weighted MR image. Then, we used the average standardized uptake value (SUV) at cerebellum as the reference to calculate the ratio between the average regional SUV and the average SUV at cerebellum (commonly called standardized uptake value ratio (SUVR)) to represent the pathological burden at each cortical region.

Resilience proxy. In this work, we use the joint product between education level and the CSF tau/A β ₄₂ ratio as the resilience proxy, since we found this interaction term manifests the role in counteracting the progression of AD in our statistical model²³.

2.3 Reaction- diffusion model

Our proposed network-guided biochemical model consists of a classic bistable model and network diffusion. This relatively simple model enabled us to investigate the spatiotemporal dynamics of ATN biomarkers in AD by capturing the essence of the underlying mechanism of complex biological phenomena. In Fig. 1B, there are four major entities in our model: (i) A biomarker (written as x_A), representing the A β protein, can be measured from Amyloid-

PET^{26,27}. (ii) T biomarker (written as \mathbf{x}_T), representing the tau protein, can be measured from Tau-PET²⁸ 1/21/22 3:33:00 PM. (iii) [N] biomarker (written as \mathbf{x}_N), measured from MRI or FDG PET, is an indicator of neuronal injury which is simplified as the damage caused by A and T biomarkers^{29–31}. (iv) A 148×148 Laplacian matrix \mathbf{L} can be calculated by subtracting the region-to-region connectivity strength from the total connectivity degree of each node, which describes the inward and outward spreading of pathological burden throughout the brain network. \mathbf{x}_A , \mathbf{x}_T , and \mathbf{x}_N are three column vectors assembling the observed degree of AT[N] biomarkers at each region.

The pathological network is an integration of AT[N] reactions and network diffusion. At each brain region, the production ((1), (3)) and clearance ((2), (4)) of amyloid and tau proteins are included in the model following zero-order and first-order mass-action kinetics, respectively. We also include the cognitive reserve proxy²³ to model the individual's network resilience (in terms of the moderated ratio of neuron loss), denoted as the inhibition pathway ((5)). The interaction of AT[N] biomarkers follows the dominant amyloid cascade hypothesis^{32,33} and is denoted as activation pathways ((6), (7)). The phenomena of damaged neurons stimulating amyloid production via reactive astrocytes³⁴ is represented by the positive feedback pathway ((8)). The classic Hill function^{35,36} is applied to approximate the multi-molecular interacting process in the activation and feedback pathways as nonlinear reactions. The part of AT[N] reactions constitute a classic bistable model. Finally, the diffusion of amyloid and tau proteins along the white matter fiber pathways in the structural brain ((9), (10)) is modeled using the graph equivalent Laplacian matrix \mathbf{L} as the diffusion operator on the brain network, where \mathbf{L} characterize the dynamic balance of influx and outflux of neuropathological burdens at each node. The diagram in Fig. 1B can be converted into three sets of PDEs (1), which model the spatiotemporal dynamics for A, T, and [N] biomarkers, respectively.

$$\left\{ \begin{array}{llll} \frac{\partial \mathbf{x}_A}{\partial t} = k_{pA} - k_{dA}\mathbf{x}_A + k_{NA} \frac{(\mathbf{x}_N)^\alpha}{k_{MN}^\alpha + (\mathbf{x}_N)^\alpha} + d_A \mathbf{L} \mathbf{x}_A & \textcircled{1} & \textcircled{2} & \textcircled{8} & \textcircled{9} \\ \frac{\partial \mathbf{x}_T}{\partial t} = k_{pT} - k_{dT}\mathbf{x}_T + k_{AT} \frac{(\mathbf{x}_A)^\beta}{K_{MA}^\beta + (\mathbf{x}_A)^\beta} + d_T \mathbf{L} \mathbf{x}_T & \textcircled{3} & \textcircled{4} & \textcircled{6} & \textcircled{10} \\ \frac{\partial \mathbf{x}_N}{\partial t} = -k_\gamma r \cdot \mathbf{x}_N + k_{TN} \frac{(\mathbf{x}_T)^\gamma}{K_{MT}^\gamma + (\mathbf{x}_T)^\gamma} & \textcircled{5} & & \textcircled{7} & \end{array} \right. \quad (1)$$

We use hyperparameter Θ to denote model parameters which are necessary to characterize the rate constants of production (k_{pA} , k_{pT}), clearance (k_{dA} , k_{dT}), activation and positive feedback (k_{NA} , k_{AT} , k_{TN}), inhibition (k_r), diffusion (d_A , d_T), dissociation (k_{MA} , k_{MT} , k_{MN}), and the coefficients in Hill function (α , β , γ). Our PDE-based model can be used to predict the evolution of AT[N] biomarkers given the baseline biomarkers, understand the complex physiopathological mechanism of AD by analyzing the system behaviors as described next.

2.4 System stability analysis

By solving the characteristic equations of our PDEs, we can find the equilibria of our model, which captures a nonlinear dynamical system on a continuous-time domain. Lyapunov's stable theory³⁷ is applied to further analyze the local stability of the detected equilibria. The equilibrium found is stable if and only if the real part of the solution to the characteristic equations or eigenvalue of the Jacobian matrix are all negative. Our bistable system generates two stable equilibria, mirroring the diagnosis of Alzheimer's disease: the small equilibrium represents the low-risk state with low accumulation of AT[N] biomarkers, and the high-risk state with high biomarker levels. The characterization of stability analysis allows us to predict the spatiotemporal evolution of AT[N] biomarkers and investigate vulnerable structures in the brain where a subtle disturbance would significantly influence the dynamics of other regions.

2.5 Parameter optimization

The receiver operating characteristic analysis was used to assess the classification of disease status using biomarker SUVR values. Subjects were first divided into two groups as: the low-energy cognitive normal state (CN, SMC, EMCI) and the high-energy AD state (LMCI, AD). An optimal cutoff value was found for each brain region by maximizing the sum of sensitivity and specificity and served as a threshold to classify individuals' regional SUVR value (from last scans) into either low or high levels. The average accuracies are 66.13%, 72.19%, 61.31% for A, T, and [N] biomarkers, respectively. The average sensitivity and specificity are 61.71% and 67.70% (A), 43.47% and 82.37% (T), 60.52% and 61.56% (N) with an average area under the curve value of 0.6519 (A), 0.6290 (T), and 0.6179 (N).

In the simulation, all neuroimaging data were scaled into [0,1] to represent the relative regional concentration of AT[N] biomarkers. The model takes the regional AT[N] biomarkers as input and outputs the estimated risk for every region of interest²⁵. The bistable attribute of our model enables it to generate simulation results: each brain region evolves into either a low-risk state or a high-risk state, where LRS indicates regions predicted to remain healthy and HRS indicates regions predicted to accumulate abnormal AT[N] burden and develop into AD lesions. The average of LRS and HRS are considered as the "prediction risk" discussed in our model. Genetic algorithm was then used to optimize the hyperparameter Θ by minimizing the difference between the neuroimage classification and simulation results^{38,39}.

2.6 Statistical analysis

All statistical analyses were performed using R. Pearson correlation coefficient was calculated to measure the degree of linear correlation between two sets of data. Two-tailed student's t-tests were used to test the significance of correlation coefficients. Two-tailed Student's t-tests were used for single comparisons between two sets of data. Statistical significance was concluded with $p\text{-value} \leq 0.05$. 95% confidence level is used for confidence intervals. Results in tables are presented as mean \pm standard error of the mean.

3. Results

Subject information. Among all processed subjects' data, we selected 320 subjects spanning the AD spectrum: cognitive normal (CN), significant memory concern (SMC), early mild cognitive impairment (EMCI), late MCI (LMCI), and AD. Selected subjects have longitudinal neuroimaging scans of Amyloid-, Tau-, FDG-PET, and DWI. Based on their diagnostic labels, 143 subjects diagnosed as CN or SMC were categorized into NC (normal control) group; 98 subjects diagnosed with EMCI were classified into MCI group; 79 subjects labeled as LMCI or AD were grouped into AD group. See *Materials and methods* section for sample selection criteria and imaging processing specification; see *Supplementary information* for demographic information and neuroimaging characteristics.

3.1 Model performance

Overall model outcomes will be evaluated with AT[N] biomarkers and clinical cognitive assessment from different aspects and significant associations are found between them, demonstrating our models' potential to uncover the heterogeneous progressive pattern of AD. We will examine individual predicted risk (proportion of high-risk state for each subject across the entire brain) and regional predicted risk (proportion of high-risk state for each brain region across all subjects).

Regional tau and neurodegeneration are stronger indicators of regional AD risks. In Fig. 2A, significant positive linear association with predicted risk are observed for whole-brain amyloid accumulation ($r^2 = 0.49$, 95% $CI = [0.45, 0.53]$) and tau depositions ($r^2 = 0.42$, 95% $CI = [0.38, 0.46]$). Similarly, we analyze the linear association between regional AT[N] levels of last scans with predicted risks. As shown in Fig. 2B, the regional amyloid level has a relatively weak linear relation with predicted risk ($r^2 = 0.07$, 95% $CI = [0.01, 0.17]$), while tau and neurodegeneration exhibit strong positive associations with significant predictive power of regional tau deposition ($r^2 = 0.64$, 95% $CI = [0.52, 0.73]$) and neurodegeneration level ($r^2 = 0.62$, 95% $CI = [0.51, 0.71]$) in risk prediction. These results align well with the current understanding that tau and neurodegeneration are more closely related to AD progression in space and time^{40,41}. Specifically, the relationship between neurodegeneration and predicted risk resembles a sigmoidal curve, implying that the initial low-level accumulation of neurodegeneration will not notably increase the risk of AD until it reaches a certain threshold¹³.

In Fig. 2C, while a similar pattern of AT[N] burden is observed, there is a clear increase of neurodegeneration accumulated in temporal and occipital lobes, suggesting that the synaptic losses are most severe in the temporal lobe during AD progression. In Fig. 2D, our predicted risk accords with averaged AT[N] patterns with an apparent increase of prediction risk in the middle and inferior temporal gyrus from the sagittal view of the brain, demonstrating the vulnerability of the temporal lobe and the indicative sign in early AD diagnosis^{11,42}. We further measure the validity of our model using clinical cognitive assessments. Our prediction risks are found to be linearly associated with Mini-Mental State Exam (MMSE) scores ($r^2 = 0.18$,

95% $CI = [0.10, 0.26]$), Clinical Dementia Rating (CDR) scores ($r^2 = 0.20$, 95% $CI = [0.13, 0.28]$), and Alzheimer's Disease Assessment Scale (ADAS) ($r^2 = 0.20$, 95% $CI = [0.12, 0.29]$), as shown in Fig. 2E.

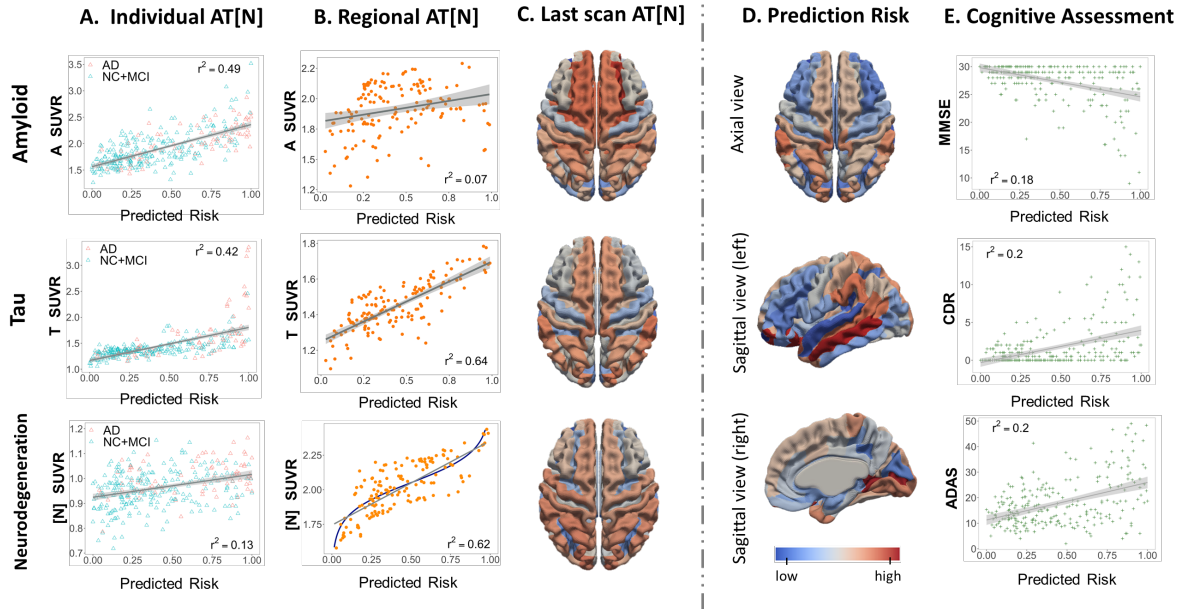


Figure 2. Model performance in prediction risk. (A) Individual predicted risk (proportion of high-risk states for each subject) vs. last scans of AT[N] biomarkers averaged over brain regions. Each triangle represents an individual subject. (B) Regional predicted risk (proportion of high-risk states for each brain region) vs. last scans of AT[N] biomarkers averaged over subjects. Each dot represents a brain region. (C) Axial views of AT[N] SUVR values averaged over subjects' last scans. (D) Surface rendering of prediction risk averaged over all 320 subjects in axial and sagittal views. The color spectrum ranges from red (high risk) to blue (low risk). (E) Individual predicted risk vs. cognitive assessments (MMSE, CDR, and ADAS).

Amyloid and tau progression patterns affect model prediction. Our primary model performance is discussed in *Results* section, which presents a strong linear relationship between AT[N] neuroimaging examinations and cognitive tests. Here we investigate our model results by examining the predictive error. By fitting the least square linear regression model of regional neurodegeneration [N] over average regional risk, regions of interest are then classified as (i) fitted prediction if the observed [N] lies within the 99% confidence interval (CI) of predictions, (ii) overestimations if the observation lies below the CI of predictions, (iii) underestimations if the observation lies above the CI (Fig. 3A). A similar pattern is detected across AT[N] biomarkers when we compare the surface rendering of neurodegeneration (Fig. 3E) with the average level of amyloid and tau over 320 subjects (Fig. 3B, F). Our model tends to overestimate the risk of AD for regions with high A and T profiles (red regions in Fig. 3B, F) and underestimate the risk of AD at regions with low A and T profiles (cyan color regions). Fig. 3C and G show the significant difference between AT levels in overestimated group and underestimated group, which confirms that overestimated regions have higher amyloid and tau burden than underestimated areas. The model residual shows a negative correlation with observed amyloid ($r^2 = 0.11$) and tau deposition ($r^2 = 0.32$), implying that the aberrant regional amyloid and tau deposition affects the model accuracy in AD risk evaluation (Fig. 3D, H).

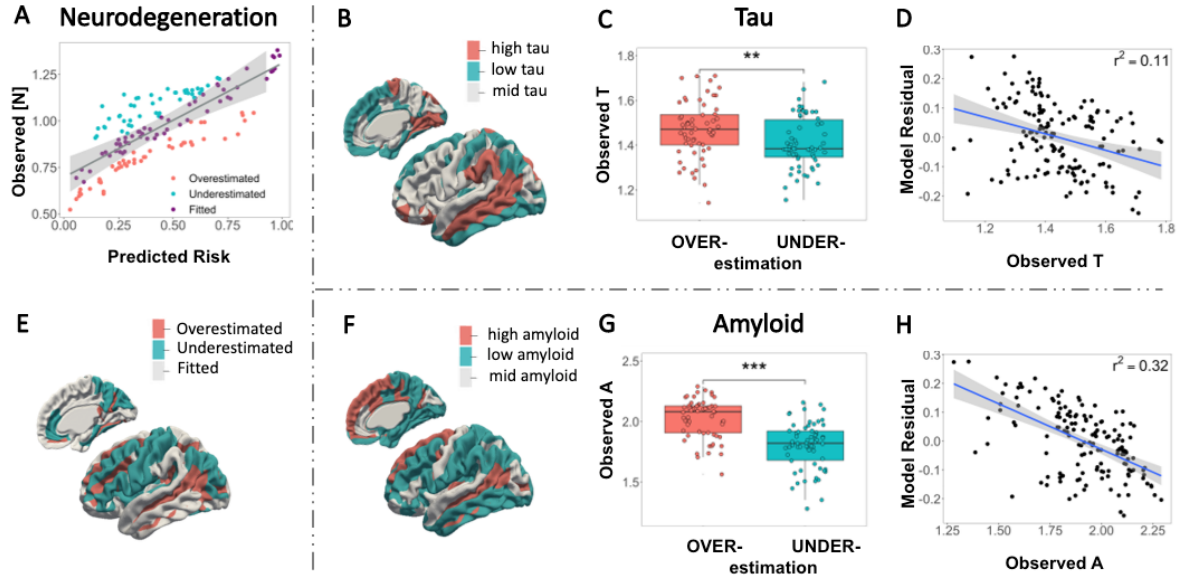


Figure 3. Amyloid and tau explain regional model under-, over-estimation. (A) Predicted risk vs. observed [N] biomarker (last scans averaged over subjects). Brain nodes are classified as overestimated or underestimated according to the sign of model residual. (E) Surface rendering of under/overestimated neurodegeneration. (B), (F) Amyloid and tau deposition pattern averaged over subjects' last scans, with red representing a high level and blue representing a low level using the optimal cutoff value. (C), (G) Boxplots of regional amyloid and tau level in under/overestimated groups. (D), (H) Correlations between regional model residual and biomarkers tau, amyloid. Negative model residuals indicate model overestimations, while positive model residuals indicate model underestimations.

3.2 System vulnerability

Studies have shown the AT[N] biomarkers tend to attack different areas of the brain^{43–45}. In Fig. 4B-D, we summarized brain regions that are frequently reported being affected in literature for A, T, and [N] biomarkers, respectively. In general, higher levels of amyloid deposition were found in the anterior cingulate, frontal cortex, lateral temporal cortex, parietal cortex, precuneus, and anterior ventral striatum in participants with mild cognitive impairment compared with normal control⁴³ (Fig. 4B). Regional Tau-PET levels revealed that tau attacked trans-entorhinal cortex, entorhinal cortex, and medial temporal limbic system heavily except for the hippocampus⁴⁵ (Fig. 4C, hippocampus is currently not included in our atlas). Regions with the drastic decline in cortical thickness ([N]) exhibit in the left anterior cingulate, dorsolateral prefrontal cortex, orbitofrontal cortex, visual association cortex, and medial temporal lobe, outlining para-hippocampal gyrus⁴⁴ (Fig. 4D). See details of brain nodes' location in literature²⁵.

Temporal and occipital lobes suffer vulnerability to pathological AD progression. To unveil brain regions vulnerable to abnormal AT[N] attacks, we perform an extensive simulation of random abnormal onset on the brain. By randomly placing abnormal malignant AT[N] onsets across brain regions, we record the nodes that reach HRS (high-risk state) after system stabilization. A group of 14 nodes is identified as most susceptible to developing into HRS regardless of the initial abnormal onset and are therefore referred to as vulnerable regions. As shown in Fig. 4E, 64.3% of vulnerable nodes locate in temporal and occipital lobes and 35.8%

of them are among the worst 10% neurodegenerative regions. Since HRS is assumed to be associated with high AT[N] profiles, we check the bar plot of regional AT[N] together with the predicted risk, sorted by the ascending risk (Fig. 4A). Concert with previous understanding, majority of nodes with higher risks have higher accumulations of amyloid, tau, and neurodegeneration. However, the AT[N] SUVR values of some vulnerable regions (such as nodes #21, #23, #41) are at a medium level, indicating that vulnerable regions do not necessarily refer to regions with the most neuropathological burdens. We further compare longitudinal changes of AT[N] level in different diagnostic groups between vulnerable regions and severely attacked regions from literature, as summarized in Fig. 4B-D. In the corresponding heatmaps, the overall increase of neuropathological burdens at vulnerable regions are higher than regions summarized from literature, especially for tau, confirming the susceptibility of vulnerable nodes and significant increases of tau level in AD development.

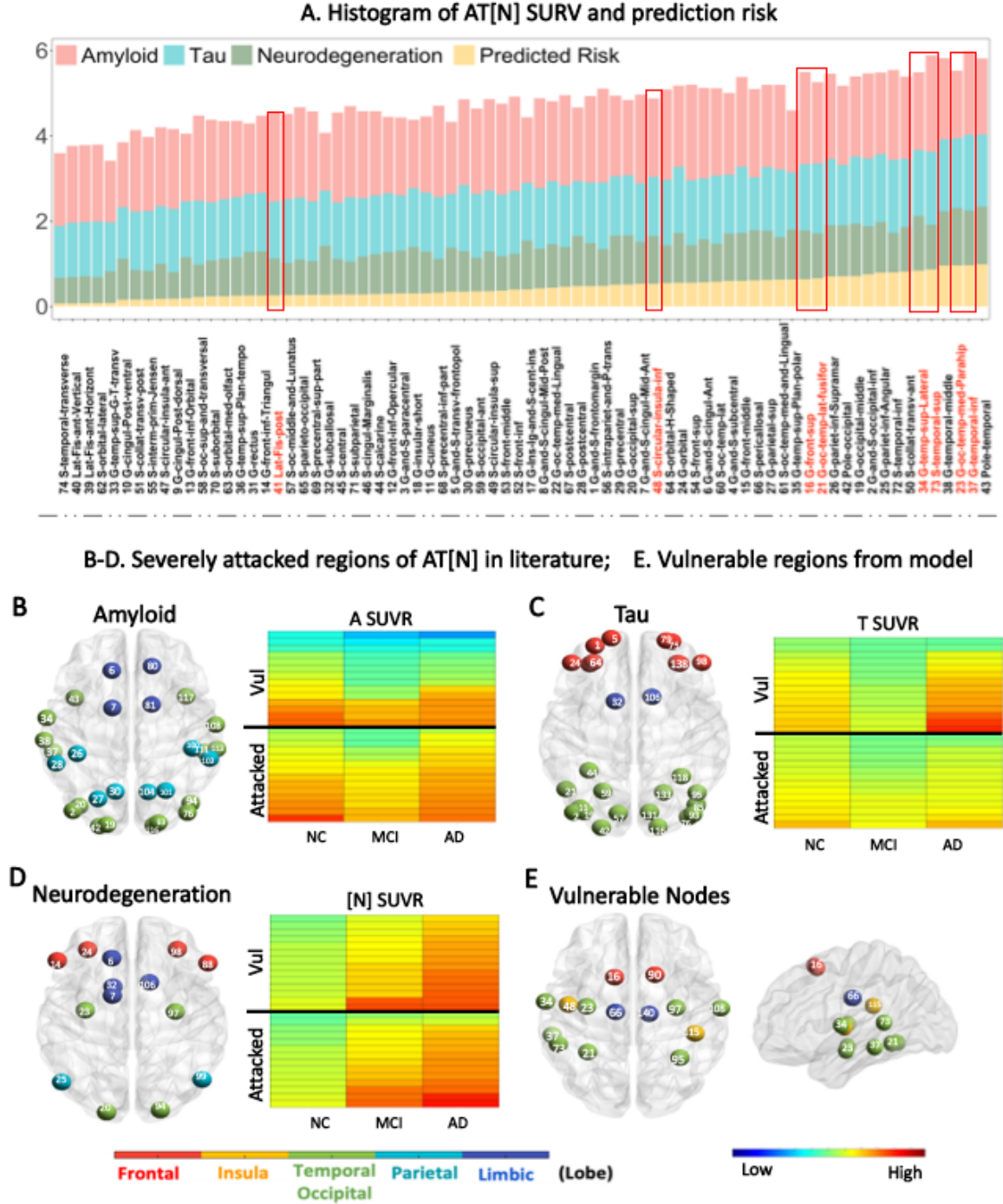


Figure 4. Vulnerable brain regions to AT[N] attack. (A) Bar plot of AT[N] SURV values and predicted risk at each node in the left hemisphere, sorted by predicted risk in ascending order. Vulnerable nodes are highlighted in red rectangles. (B)-(D) Brain mapping of severely attacked regions for amyloid, tau, neurodegeneration from literature. Heatmaps of AT[N] longitudinal changes between last scan and first scan for NC, MCI, and AD groups. Top 14 severely attacked regions and vulnerable brain regions are shown in comparison and sorted by the difference of SURV level in ascending order. (E) Vulnerable regions detected by our model. Ball colors indicate different brain lobes.

3.3 System criticality

Besides vulnerable regions that are susceptible to abnormal AT[N] attacks, we are also interested in regions that are capable of spreading AT[N] burden and are critical to whole-brain

AD development. Considering the diffusive nature of AT biomarkers, critical regions are expected to be transmissible to disease factors, where subtle increases can quickly spread out and significantly affect neighboring and further areas. Many researchers in AD field have proposed different sets of “hub nodes” in brain networks aiming to demonstrate their prominent role in AD progression^{46,47}. We nominate a set of critical nodes that are most influential in pathological progression across the brain based on our biochemical model, which would shed light on precision medicine and early prediction in AD field.

Regional onset of critical nodes outperforms hub nodes. For the selection of critical brain regions, we increase the AT[N] levels for random groups of nodes, count the number of brain regions that end up at HRS after system stabilization, and choose the set of nodes that convert most brain regions into HRS. Fig. 5 presents the comparison between our proposed critical nodes (Fig. 5C) with hub nodes (Fig. 5B) from literature⁴⁷ and a set of randomly selected nodes (Fig. 5A), where hub nodes and critical nodes coincides in the region of bilateral orbital gyri. By tuning the three sets of nodes (blue nodes) to abnormal levels and keeping the rest as normal, we evaluate the transmissibility of disease factors for those nodes. Critical nodes impact and drive as much as 49 nodes to HRS (Fig. 5F), whereas hub nodes and random nodes affect 29 nodes (Fig. 5E) and 24 nodes (Fig. 5D), respectively. The predicted risks of critical nodes are larger than 0.7 in left and right inferior temporal gyrus, left and right superior temporal gyrus, and left supramarginal gyrus. This finding is consistent with the previous study that temporal gyrus, which plays a major role in object recognition, is one of cognitive functions that are impaired early on in AD^{48,49}.

Further, we investigate the graph-theoretic metrics: degree, PageRank, and closeness centrality for each region of interest (ROI) across all subjects. In Fig. 5G-I, we compare the overall degree (a measure of connectivity strength), closeness centrality (a measure of how long it will take to spread information sequentially from the current node to all other nodes), and PageRank (an identification of influential nodes whose influence extends beyond their direct connections). Overall, critical nodes and hub nodes have similar degrees (Fig. 5G), PageRank (Fig. 5H), and closeness (Fig. 5I) and are both higher than the random nodes. Even though there are some hub nodes with notable higher degrees, PageRank, and closeness (which are reasonable as they are selected based on those metrics), the critical regions outperform hubs nodes and impact much more brain regions. This indicates that brain network structure is an important but not the only factor influencing AD transmission and progression.

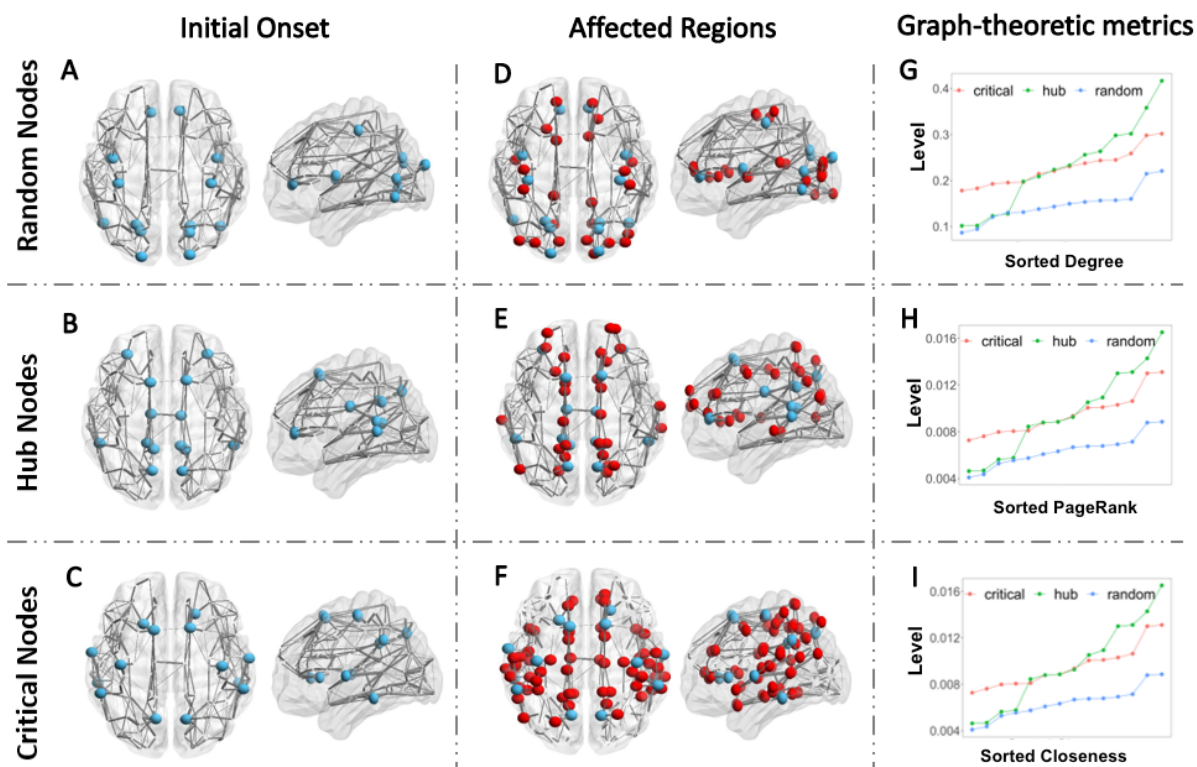


Figure 5. Regional onset of critical brain regions compared with hub nodes and random nodes. (A)-(C) Initial regional onset of randomly selected nodes, hub nodes, and critical nodes. (D)-(F) Predicted brain regions under high risk using random nodes onset, hub nodes onset, and critical nodes onset. Blue balls indicate the location of random nodes, hub nodes, and critical nodes; red balls are brain regions affected and developed to high-risk state; grey lines represent an averaged brain network with its thickness denoting the relative region-to-region connectivity strength. (G)-(I) Graph-theoretic metrics of degree, PageRank, and closeness centrality (sorted in ascending order) at random nodes, hub nodes, and critical nodes, respectively.

3.4 Pathway and network influence

To better understand the influential roles of various pathways in our network-guided model, we examine the system behaviors under different amyloid and tau production, clearance, activation, and diffusion rates (See *Materials and methods* for detailed descriptions of mechanistic pathways).

Overproduction and clearance deficiency of amyloid and tau significantly increase AD risk. Minor abnormalities in amyloid and tau usually can be self-corrected by neurons through different cleaning mechanisms such as proteolytic degradation and out-of-brain transportation via blood-brain barrier^{2,50}. However, AD patients are unable to restrain these disease factors within the normal range due to their disrupted production-clearance balance^{20,51}. To test the clinical impact of this metabolic balance, we experimentally vary the rate constants of reactive pathways in our system and trace the changes in predictive risk for each clinical diagnosis (NC, MCI, AD). We find a clear stratification among different diagnostic labels where the predicted risk in AD group scores higher than MCI and NC, see Fig. 6A-H. We also observe a statistically significant difference in predicted risks among varied production rates and clearance rates of AT (Fig. 6A, B, E, F). The changes in amyloid and tau production rates explain about 8% (r^2)

and 17.7% of the increase in predicted risk, respectively; the changes in amyloid and tau clearance rates explain 24.5% and 20.3% of the decrease in predicted risk. These suggest that elevated production rate and suppressed clearance rate will significantly increase the risk of AD.

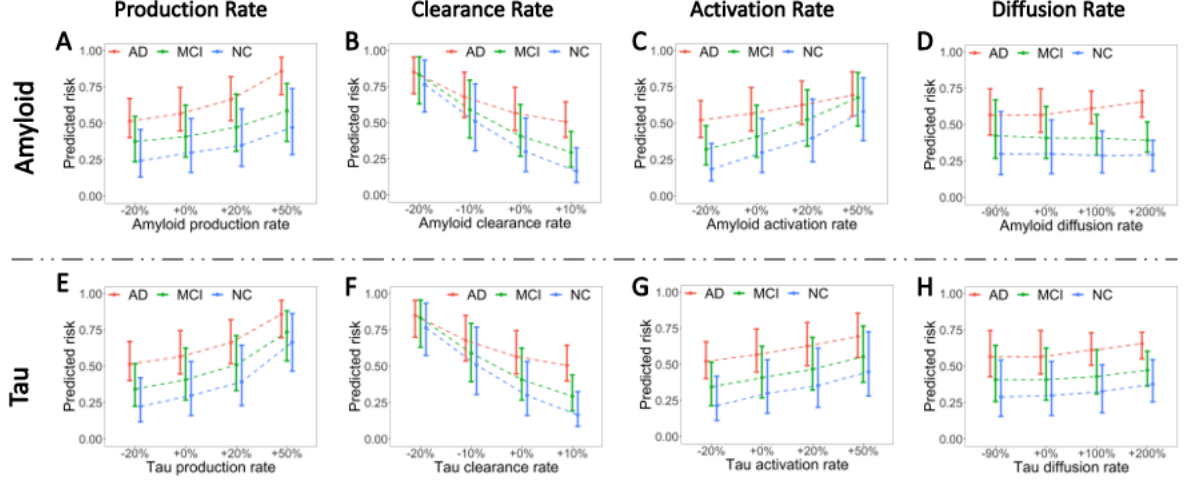


Figure 6. Influence of amyloid and tau production, clearance, activation, and diffusion rates. (A)-(H) Predicted risk with varied reaction rate constants. For each plot, bars indicate the 25 and 75 percentiles of predicted risk, and the dashed line connects the mean of predicted risk under different reaction rates. The x-axis represents the relative increase (+) or decrease (-) of rate constants. +0% is the base reaction rate used in the model. The colors denote the diagnostic labels of each group (NC, MCI, AD).

We then check the effect of activation and diffusion for amyloid and tau. A similar stratified risk level is observed between different clinical labels: AD groups have the highest risk, followed by MCI and NC. For the activation pathway, a general rising pattern of risk is witnessed in both amyloid and tau as we increase the rate constant (see Fig. 6C, G). When increasing the activation rate by 50%, the risks from the three groups overlap, indicating the hyper-active amyloid and tau may lead to high risk regardless of subjects' diagnostic stage. The changes in amyloid and tau activation rate explain 12% and 6% of the increase in predicted risk, respectively. It is worth noting that there is no significant increase (0.006% and 1%) of risk prediction when we double or even triple the diffusion rate for amyloid and tau (Fig. 6D, H). Even though network connectivity is recognized as a critical factor in AD, scaling up the diffusion rate alone may accelerate the speed of disease progression but do not change the final disease stage, and thus is not influential to predicted risk here.

3.5 System stability

Since a high reaction rate usually indicates a rapid disease progression, it is fundamental to investigate when the disease will evolve into a stable stage (remains in NC or AD), which can be characterized by the system time it takes to reach equilibria (steady state) from the initial condition. Like the previous setting, we track the stability time under different rate constants of production, clearance, activation, and diffusion for amyloid and tau. Compared to amyloid, tau presents more variations in stability time when the production rate is tuned up by 50% (Fig.

7A), the clearance rate is down by 20% (Fig. 7B), or when the diffusion rate is tripled (Fig. 7D). We also observe a positive association between tau activation rate and stability time (Fig. 7C), illustrating the vital role of tau hyperphosphorylation in AD progression.

Characteristic time of system stability varies with diagnostic stages. We further examine the influence of structural networks on disease progression. Although some outliers affect the fitting performance, we observe positive associations between connectivity strength and stability time (the system time it takes to reach a steady state from the initial condition) across all groups in Fig. 7E. Nodes with lower connectivity strength tend to reach stable states faster. The dynamics of network diffusion alone can also be characterized by the second eigenvalue of the graph Laplacian matrix, denoted as λ_2 , which dominates the convergence speed to steady state or system equilibrium. Fig. 7F displays the bootstrap distribution of “relaxation time” ($1/\lambda_2$), an essential measurement of the time scale for a system to return to its steady state after a perturbation. A larger relaxation time (as seen with the AD group) indicates a longer diffusion process and therefore may lead to longer-lasting damage due to increased duration of amyloid or tau presence.

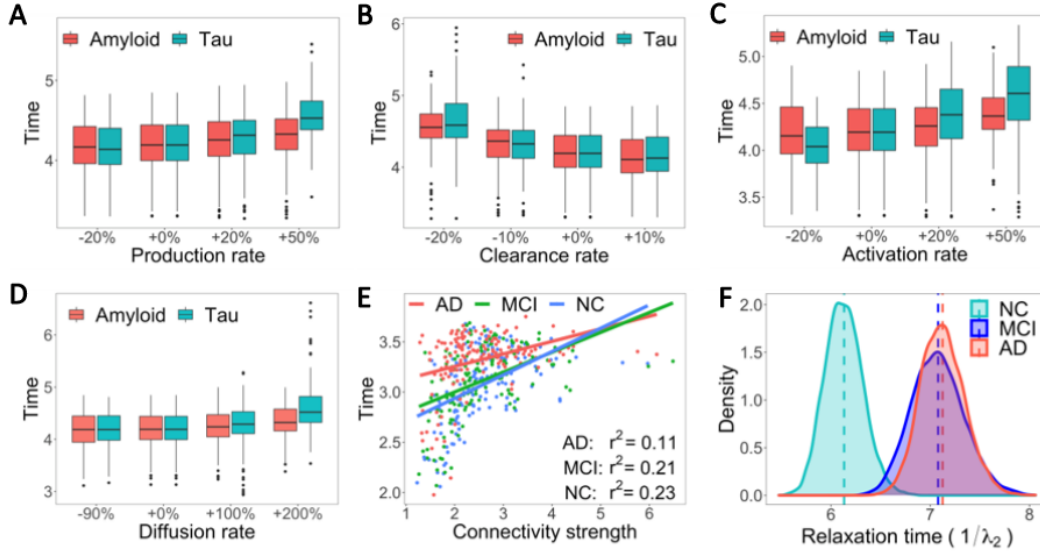


Figure 7. Influence of amyloid and tau production, clearance, activation, and diffusion rates on stability time. (A)-(D) Boxplots of stability time with varied rate constants of production, clearance, activation, and diffusion. The x-axis represents the relative increase (+) or decrease (-) of rate constants. +0% is the base reaction rate used in the model. The y-axis represents the time that the system takes to reach a stable state. (E) Linear regression fitting of connectivity strength over stability time (the time to reach system equilibrium) for each diagnostic group. (F) Bootstrap distribution of relaxation time (inverse of the second eigenvalue of Laplacian matrix, or convergence speed to system equilibrium) for each group.

3.6 Braak-like spreading pattern

Inspired by a wealth of preclinical *in vivo* and *in vitro* research in the past decade that amyloid and tau proliferation in the brain follows a prion-like pattern transmitting between neurons^{19,52,53}, we will use our model to examine the general spread pattern. According to Braak⁵⁴, amyloid progression can be divided into three stages (Stages I~III) and the development of tau is summarized into six stages (Stages I~VI). In the early stages (I, II) of

tau, as shown in Fig. 8H, the mild affection of neurofibrillary tangles and neuropil threads (NT) are confined to the trans-entorhinal region. The entorhinal and trans-entorhinal regions are severely impacted by NFT and NT at middle stages (III, IV). At the late stages (V, VI), all parts of the hippocampal formation are attacked and NFT with long extension reaches the outer part of the iso-cortex. The progression of amyloid falls into a relatively reversed pattern compared with Tau (see Fig. 8D). In the early stage of AD (I), low levels of amyloid are depositing in the iso-cortex. Medium densities of amyloid are spread into almost all iso-cortical associated regions. The late stage of AD (III) is characterized by loads of amyloid in the entire iso-cortical regions⁵⁴.

The overall progression of amyloid and tau follow the Braak-like pattern across the brain. By placing the abnormal disease factors at the early Braak stage, our model likewise simulates the Braak-like spread patterns of amyloid and tau across the brain. As we can see from Fig. 8A-C, amyloid first deposits over fronto-medial and temporo-basal areas and disperses into the adjacent iso-cortex. Amyloid then severely attacks the remaining associative neocortex. It arrives at the striatum at the final stage, leaving the entire brain affected. Fig. 8E-G has revealed a similar spread pattern as Braak staging of tau. Tau first spreads from entorhinal and trans-entorhinal regions to para-hippocampal, fusiform, amygdala, and related regions. From there, tau accumulates across the entire iso-cortex and brain.

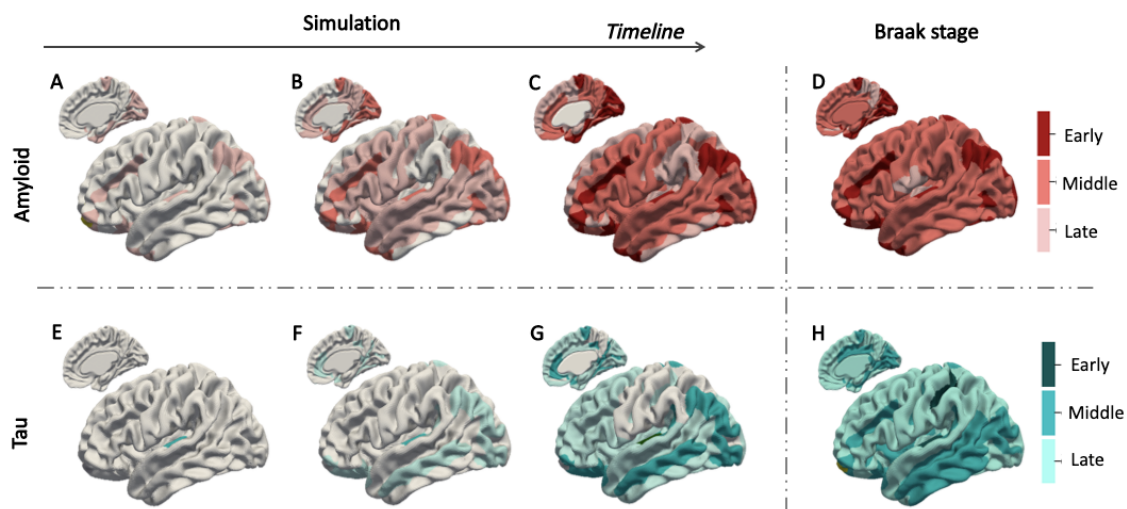


Figure 8. Spread pattern of amyloid and tau in our model and Braak stages. (A), (E) Initial onset of abnormal amyloid (red) and tau (green). (B), (F) Progressive pattern of AT at the middle stage of simulation. (C), (G) Final pattern of AT accumulation across the brain at the end of simulation, when the system arrives at the stable state. (D), (H) Prion-like transmitting pattern between neurons of AT proposed by Braak. The dark to light spectrum of red/green represents early, middle, and late stages of amyloid/tau Braak staging.

4. Discussion

Alzheimer's disease is irreversible and slowly progressive dementia with limited treatments. Due to the multiplicity of clinical symptoms, standard neuropsychological assessments inadequately reflect the underlying pathophysiological mechanisms, rendering a significant

gap between neurobiological examinations of AD pathology and clinical diagnoses. The in-depth understanding of how AT[N] biomarkers spread throughout the brain is a crucial step because disentangling the regions that are vulnerable to the attack of disease factors and the regions that are highly “contagious” after suffering from abnormal accumulation of those neuropathological burdens is the gateway for precision medicine. Based on our previous model⁵⁵, we processed considerable neuroimaging data from two-fold individual subjects, added in longitudinal Tau-PET data, and replaced original MRI data with fluorodeoxyglucose PET for more accurate measurement of neurodegeneration. The baseline and final scans of Amyloid-, Tau-, and FDG-PET are used as initial and final indicators of AT[N] biomarker levels accordingly.

While AT[N] biomarkers are considered pathological hallmarks of Alzheimer’s disease, none of them is unique to Alzheimer’s disease. To make the situation more complex, high-level amyloid, tau, and neurodegeneration accumulations are not limited to AD subjects but also exist in some normal aging populations. Thus, measurement of AT[N] level alone is insufficient for clinical diagnosis and a universal cutoff value for biomarker abnormality might be inaccurate for classification. A well-designed model is in demand to differentiate normal accumulation and pathological progression. In this study, we employ the proposed network-guided reaction-diffusion model to analyze the impact of biomarker interactions and network diffusion on AD progression. Our model performance is evaluated using the R-squared (coefficient of determination) between the AT[N] levels and our predicted risk (Fig. 2A, B). Since the simulation results are governed by the reaction-diffusion model, we further evaluate the correlation between the global attribute of system behaviors (the percentile of predicted high-risk regions) and cognitive measurements (CDR, ADAS, and MMSE), which all exhibits significant positive relationships ($p < 10^{-16}$), as shown in Fig. 2E. Such a noticeable association between system behaviors and clinical outcomes shows the potential of our model in disentangling the heterogeneity of neurodegeneration trajectories.

While our model results are accurate on a general view, over- or under-estimations do occur with high and low regional AT burdens. Certain nodes with higher regional amyloid and tau deposition tend to have low neurodegeneration which leads to an over-estimation by our model. The spatial concurrence of AT[N] biomarkers could explain this prediction error as abnormal amyloid and tau deposition is associated with and can accelerate neurodegeneration^{9,40,41}. This urges the need to include more longitudinal AT[N] biomarkers in model construction as they provide more comprehensive information on the underlying microscale disease progression. Notice that the simplification of our model might also contribute to this estimation error. Our current model does not account for the “incubation time” from the build-up of amyloid to the onset of tau pathology, either to the onset of neurodegeneration and clinical dementia. It is worth mentioning that, along with other studies^{40,56}, we found that the average time lapse between low to high amyloid transition ($A^- \rightarrow A^+$) and low to high neurodegeneration transition ($[N]^- \rightarrow [N]^+$) could be as long as 18 months in the ADNI dataset. The inclusion of temporal latency in future modeling could potentially improve the overall accuracy of AT[N] biomarker evolution.

Extensive research has proven the detrimental effects of mitochondria functionality, oxidative stress, long-term potentiation, synaptic plasticity, and memory caused by the irregularity of beta-amyloid^{1,2}. Yet these potential disease factors can be maintained at a normal

level through different clearance mechanisms, including proteolytic degradation, out-of-brain transportation via blood-brain barrier, immune responses, and protein-mediation^{2,20,57}. If the metabolic balance is interrupted, either through overproduction or clearance deficiency, a chain of downstream consequences will be triggered, and eventually leads to AD. This conclusion is backed by our model results with tuned parameters of amyloid and tau. Increasing the production rate or decreasing the clearance rate can cause a notable rise in predicted risk. When reducing the clearance rates of amyloid or tau node by 20%, all regions surge in the high-risk range regardless of clinical diagnostic label, indicating that the interrupted metabolic balance may be a key to the initiation and progression of Alzheimer's disease^{51,58,59}.

Recent research shows the critical role of brain network during the evolution of Alzheimer's disease. Several laboratory studies showed that hyperphosphorylated tau would spread along with structural brain networks, leading to neuron loss^{11,60}. Our study, however, reveals that the final predicted risk will not be affected if we increase the diffusion rate alone. While it could be partially explained by the measurement error during neuroimaging acquisition and data processing, the static brain network could play a significant role here. In our model, we used the average network connectivity of each diagnostic group (NC, MCI, and AD) to simulate individuals' AT[N] dynamics. Since the neurodegenerative process could alter the network topology⁶¹, network alteration might likely manifest a dynamic propagation of pathological burdens. We can incorporate subject-specific longitudinal brain networks in the study to further examine the influence of network alternation in disease progression.

With an extensive search via randomly seeding amyloid and tau disease factors, we found the temporal lobe, especially the middle and inferior temporal gyrus, suffers great vulnerability to abnormal AT disposition. Unlike traditional studies, our work shows the brain regions that are affected most by abnormal AT[N] attacks are not constraint to regions with high amyloid or tau depositions. Some regions, such as the fusiform gyrus and parahippocampal gyrus, bear average AT burdens are at high risk to neuropathological alternation caused by AD, encouraging more attention to those regions for clinical diagnosis and treatment. Besides vulnerability, our model also reveals that bilateral inferior temporal gyrus, bilateral superior temporal gyrus, and left supramarginal gyrus are exceptionally transmissible to AT[N] attack during Alzheimer's progression. The criticality of those brain regions provides insights on new interpretation of neuroimaging data in AD diagnosis and advocates early treatments on those particular sites to delay or prevent potential future whole-brain AD development.

Our analyses on empirical data reveal a concurrent progression of T[N] biomarkers and a strong indicative power of T[N] profiles in AD prediction. Based on the proposed systems biology model, we proved the importance of maintaining the metabolic balance of amyloid and tau in AD prevention and targeting temporal lobe in clinical intervention. More importantly, our findings of vulnerable regions that are severely attacked by and critical regions that are highly contagious to AT[N] profiles would shed light on early AD prediction and precision medicine. Future work in considering delayed pathways and network alteration may further improve our model framework and accuracy.

Declarations of interest

The authors declare that there is no conflict of interest.

Author's contributions

Jingwen Zhang: Conceptualization, Methodology, Formal analysis, Investigation, Data Curation, Visualization, Writing - Original Draft. **Qing Liu:** Methodology, Formal analysis, Writing - Review & Editing. **Haorui Zhang:** Data Curation, Validation, Visualization. **Michelle Dai:** Conceptualization, Investigation, Validation, Writing - Original Draft. **Qianqian Song:** Validation, Writing- Review & Editing. **Defu Yang:** Conceptualization, Data Processing, Resources. **Guorong Wu:** Conceptualization, Methodology, Resources, Validation, Writing - Review & Editing, Supervision. **Minghan Chen:** Conceptualization, Methodology, Validation, Resources, Writing - Review & Editing, Supervision.

Supplementary information

Subject demographics and biomarker characteristics

The demographic information of studied subjects is summarized in Supplementary Table 1, where we observe (i) a slowdown of amyloid deposition in AD group, (ii) a notable low deposition of tau in MCI group, and (iii) an increase of neurodegeneration from NC to AD group.

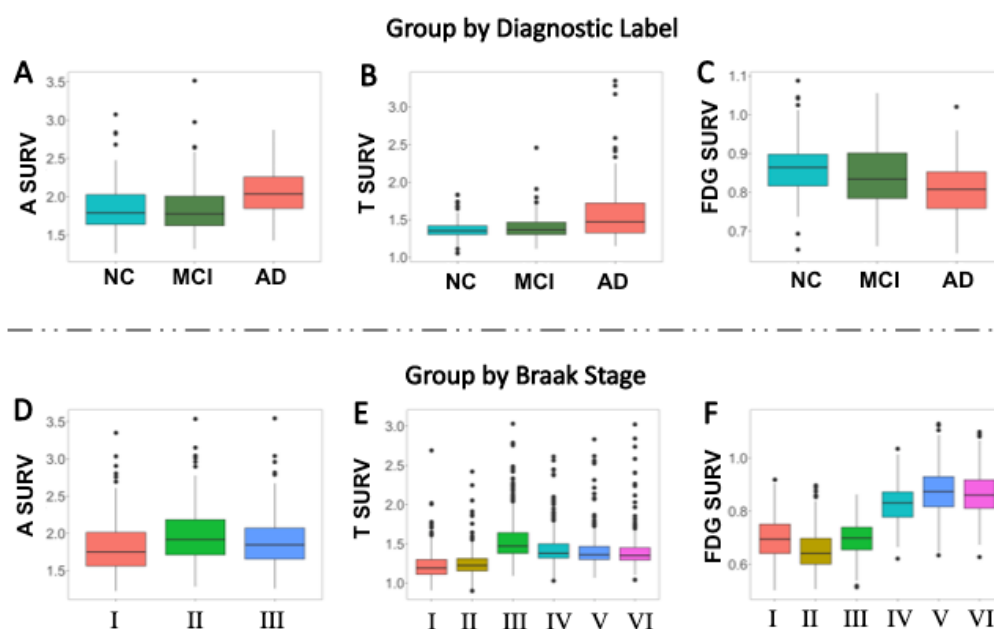
Supplementary Table 1. Demographics and biomarker characteristics.

Subject category Subject number	NC 143	MCI 98	AD 79
Gender (M/F)	66/77	60/38	47/32
Age (year)	72.99 ± 6.56	71.96 ± 6.94	73.93 ± 7.79
Education (year)	16.68 ± 2.27	16.47 ± 2.73	16.23 ± 2.81
ΔAmyloid (node avg.)	0.06 ± 0.02	0.06 ± 0.02	0.05 ± 0.03
ΔTime (month)	59.81 ± 27.00	54.31 ± 27.49	45.48 ± 25.34
ΔTau (node avg.)	0.03 ± 0.01	0.01 ± 0.02	0.03 ± 0.02
ΔTime (month)	22.11 ± 8.63	21.19 ± 10.11	20.49 ± 9.72
ΔFDG (node avg.)	-0.02 ± 0.01	-0.02 ± 0.01	-0.03 ± 0.01
ΔTime (month)	38.75 ± 25.45	40.87 ± 24.75	36.26 ± 24.04

Δ represents the change of biomarker SUVR values or time interval from first scans to last scans.

Distribution of AT[N] biomarkers

We first analyze the distribution of AT[N] biomarker levels among different diagnostic groups (NC, MCI, and AD), shown in Supplementary Fig. 1A-C. The overall median and interquartile range show an increasing trend from the boxplots of amyloid and tau; while FDG presents a reversed pattern, as it is the opposite indicator of neurodegeneration. According to Braak stage³⁹, amyloid progression can be divided into three stages (Stages I~III) and the development of tau is summarized into six stages (Stages I~VI). In Supplementary Fig. 1D and E, both amyloid and tau exhibit an increase-decrease pattern, with the highest accumulation in middle stages. In Supplementary Fig. 1F, the neurodegeneration level is consistent with Braak stages where it occurs most at the beginning stages I, II (low FDG) and gradually decreases in stages IV-VI (high FDG).



Supplementary Figure 1. Statistical analysis of AT[N] biomarkers at each clinical diagnostic group and Braak stage. (A)-(C) Distributions of amyloid, tau, and FDG SUVR values for three diagnostic groups (NC, MCI, AD). (D)-(F) Distributions of amyloid, tau, and FDG SUVR values at different Braak stages, with color representing each Braak stage. Reversed FDG is used as an indicator for [N] biomarker.

References

1. Jack CR, Bennett DA, Blennow K, et al. NIA-AA Research Framework: Toward a biological definition of Alzheimer's disease. *Alzheimers Dement*. 2018;14(4):535-562. doi:<https://doi.org/10.1016/j.jalz.2018.02.018>
2. Chen G-F, Xu T-H, Yan Y, et al. Amyloid beta: structure, biology and structure-based therapeutic development. *Acta Pharmacol Sin*. 2017;38(9):1205-1235. doi:10.1038/aps.2017.28

3. Hardy JA, Higgins GA. Alzheimer's disease: the amyloid cascade hypothesis. *Science*. 1992;256(5054):184-186.
4. LaFerla FM, Green KN, Oddo S. Intracellular amyloid- β in Alzheimer's disease. *Nat Rev Neurosci*. 2007;8(7):499-509. doi:10.1038/nrn2168
5. Ballatore C, Lee VM-Y, Trojanowski JQ. Tau-mediated neurodegeneration in Alzheimer's disease and related disorders. *Nat Rev Neurosci*. 2007;8(9):663-672. doi:10.1038/nrn2194
6. Goedert M. Tau protein and the neurofibrillary pathology of Alzheimer's disease. *Trends Neurosci*. 1993;16(11):460-465. doi:10.1016/0166-2236(93)90078-Z
7. Crews L, Masliah E. Molecular mechanisms of neurodegeneration in Alzheimer's disease. *Hum Mol Genet*. 2010;19(R1):R12-R20. doi:10.1093/hmg/ddq160
8. Kg M, W S, V O, et al. Decreased clearance of CNS beta-amyloid in Alzheimer's disease. *Science*. 2010;330(6012):1774-1774. doi:10.1126/science.1197623
9. Musiek ES, Holtzman DM. Three dimensions of the amyloid hypothesis: time, space and "wingmen." *Nat Neurosci*. 2015;18(6):800-806. doi:10.1038/nn.4018
10. Busche MA, Hyman BT. Synergy between amyloid- β and tau in Alzheimer's disease. *Nat Neurosci*. 2020;23(10):1183-1193. doi:10.1038/s41593-020-0687-6
11. Raj A, LoCastro E, Kuceyeski A, Tosun D, Relkin N, Weiner M. Network Diffusion Model of Progression Predicts Longitudinal Patterns of Atrophy and Metabolism in Alzheimer's Disease. *Cell Rep*. 2015;10(3):359-369. doi:10.1016/j.celrep.2014.12.034
12. Spires-Jones TL, Hyman BT. The Intersection of Amyloid Beta and Tau at Synapses in Alzheimer's Disease. *Neuron*. 2014;82(4):756-771. doi:10.1016/j.neuron.2014.05.004
13. Bertsch M, Franchi B, Marcello N, Tesi MC, Tosin A. Alzheimer's disease: a mathematical model for onset and progression. *Math Med Biol J IMA*. 2017;34(2):193-214. doi:10.1093/imammb/dqw003
14. Maccioni RB, Farías G, Morales I, Navarrete L. The Revitalized Tau Hypothesis on Alzheimer's Disease. *Arch Med Res*. 2010;41(3):226-231. doi:10.1016/j.arcmed.2010.03.007
15. Hardy J. The amyloid hypothesis for Alzheimer's disease: a critical reappraisal. *J Neurochem*. 2009;110(4):1129-1134. doi:https://doi.org/10.1111/j.1471-4159.2009.06181.x
16. Selkoe DJ, Hardy J. The amyloid hypothesis of Alzheimer's disease at 25 years. *EMBO Mol Med*. 2016;8(6):595-608. doi:10.15252/emmm.201606210
17. Maccioni RB, Muñoz JP, Barbeito L. The Molecular Bases of Alzheimer's Disease and Other Neurodegenerative Disorders. *Arch Med Res*. 2001;32(5):367-381. doi:10.1016/S0188-4409(01)00316-2

18. Vogel JW, Iturria-Medina Y, Strandberg OT, et al. Spread of pathological tau proteins through communicating neurons in human Alzheimer's disease. *Nat Commun.* 2020;11(1):2612. doi:10.1038/s41467-020-15701-2
19. Raj A, Kuceyeski A, Weiner M. A Network Diffusion Model of Disease Progression in Dementia. *Neuron.* 2012;73(6):1204-1215. doi:10.1016/j.neuron.2011.12.040
20. Iturria-Medina Y, Sotero RC, Toussaint PJ, Evans AC, Initiative and the Alzheimer's diseaseN. Epidemic Spreading Model to Characterize Misfolded Proteins Propagation in Aging and Associated Neurodegenerative Disorders. *PLOS Comput Biol.* 2014;10(11):e1003956. doi:10.1371/journal.pcbi.1003956
21. Bertsch M, Franchi B, Tesi MC, Tosin A. Well-posedness of a mathematical model for Alzheimer's disease. *ArXiv170905671 Math.* Published online January 5, 2018. doi:10.1137/17M1148517
22. Hao W, Friedman A. Mathematical model on Alzheimer's disease. *BMC Syst Biol.* 2016;10(1):108. doi:10.1186/s12918-016-0348-2
23. Zhang Y, Hao Y, Li L, Xia K, Wu G, Alzheimer's Disease Neuroimaging Initiative. A Novel Computational Proxy for Characterizing Cognitive Reserve in Alzheimer's Disease. *J Alzheimers Dis JAlzheimer's disease.* 2020;78(3):1217-1228. doi:10.3233/JAlzheimer's disease-201011
24. Reuter M, Schmansky NJ, Rosas HD, Fischl B. Within-subject template estimation for unbiased longitudinal image analysis. *Neuroimage.* 2012;61(4):1402-1418. doi:10.1016/j.neuroimage.2012.02.084
25. Destrieux C, Fischl B, Dale A, Halgren E. Automatic parcellation of human cortical gyri and sulci using standard anatomical nomenclature. *NeuroImage.* 2010;53(1):1-15. doi:10.1016/j.neuroimage.2010.06.010
26. Rowe CC, Ellis KA, Rimajova M, et al. Amyloid imaging results from the Australian Imaging, Biomarkers and Lifestyle (AIBL) study of aging. *Neurobiol Aging.* 2010;31(8):1275-1283. doi:10.1016/j.neurobiolaging.2010.04.007
27. Wolk DA, Price JC, Saxton JA, et al. Amyloid imaging in mild cognitive impairment subtypes. *Ann Neurol.* 2009;65(5):557-568. doi:10.1002/ana.21598
28. Hostetler ED, Walji AM, Zeng Z, et al. Preclinical Characterization of 18F-MK-6240, a Promising PET Tracer for In Vivo Quantification of Human Neurofibrillary Tangles. *J Nucl Med Off Publ Soc Nucl Med.* 2016;57(10):1599-1606. doi:10.2967/jnumed.115.171678
29. Devanand DP, Mikhno A, Pelton GH, et al. Pittsburgh compound B (11C-PIB) and fluorodeoxyglucose (18 F-FDG) PET in patients with Alzheimer disease, mild cognitive impairment, and healthy controls. *J Geriatr Psychiatry Neurol.* 2010;23(3):185-198. doi:10.1177/0891988710363715
30. Foster NL, Heidebrink JL, Clark CM, et al. FDG-PET improves accuracy in distinguishing frontotemporal dementia and Alzheimer's disease. *Brain J Neurol.* 2007;130(Pt 10):2616-2635. doi:10.1093/brain/awm177

31. Gong G, He Y, Chen ZJ, Evans AC. Convergence and divergence of thickness correlations with diffusion connections across the human cerebral cortex. *NeuroImage*. 2012;59(2):1239-1248. doi:10.1016/j.neuroimage.2011.08.017
32. Jack CR, Knopman DS, Jagust WJ, et al. Hypothetical model of dynamic biomarkers of the Alzheimer's pathological cascade. *Lancet Neurol*. 2010;9(1):119-128. doi:10.1016/S1474-4422(09)70299-6
33. Jack CR, Holtzman DM. Biomarker modeling of Alzheimer's disease. *Neuron*. 2013;80(6):1347-1358. doi:10.1016/j.neuron.2013.12.003
34. Frost GR, Li Y-M. The role of astrocytes in amyloid production and Alzheimer's disease. *Open Biol*. 2017;7(12):170228. doi:10.1098/rsob.170228
35. Goutelle S, Maurin M, Rougier F, et al. The Hill equation: a review of its capabilities in pharmacological modelling. *Fundam Clin Pharmacol*. 2008;22(6):633-648. doi:10.1111/j.1472-8206.2008.00633.x
36. Weiss JN. The Hill equation revisited: uses and misuses. *FASEB J*. 1997;11(11):835-841. doi:10.1096/fasebj.11.11.9285481
37. LaSalle J, Lefschetz S. *Stability by Lyapunov's Second Method with Applications*. Academic Press; 1960.
38. Goldberg DE. *Genetic Algorithms in Search, Optimization & Machine Learning*. Addison-Wesley; 1989.
39. Conn AR, Gould NIM, Toint P. A Globally Convergent Augmented Lagrangian Algorithm for Optimization with General Constraints and Simple Bounds. *SIAM J Numer Anal*. 1991;28(2):545-572. doi:10.1137/0728030
40. Liu Q, Yang D, Zhang J, Wei Z, Wu G, Chen M. Analyzing The Spatiotemporal Interaction And Propagation Of Atn Biomarkers In Alzheimer's Disease Using Longitudinal Neuroimaging Data. In: *2021 IEEE 18th International Symposium on Biomedical Imaging (ISBI)*. ; 2021:126-129. doi:10.1109/ISBI48211.2021.9434021
41. Ossenkoppele R, Schonhaut DR, Schöll M, et al. Tau PET patterns mirror clinical and neuroanatomical variability in Alzheimer's disease. *Brain*. 2016;139(5):1551-1567. doi:10.1093/brain/aww027
42. Veitch DP, Weiner MW, Aisen PS, et al. Understanding disease progression and improving Alzheimer's disease clinical trials: Recent highlights from the Alzheimer's Disease Neuroimaging Initiative. *Alzheimers Dement*. 2019;15(1):106-152. doi:10.1016/j.jalz.2018.08.005
43. Mathis CA, Kuller LH, Klunk WE, et al. In vivo assessment of amyloid- β deposition in nondemented very elderly subjects. *Ann Neurol*. 2013;73(6):751-761. doi:10.1002/ana.23797
44. Lerch JP, Pruessner JC, Zijdenbos A, Hampel H, Teipel SJ, Evans AC. Focal decline of cortical thickness in Alzheimer's disease identified by computational neuroanatomy. *Cereb Cortex N Y N 1991*. 2005;15(7):995-1001. doi:10.1093/cercor/bhh200

45. Franzmeier N, Rubinski A, Neitzel J, et al. Functional connectivity associated with tau levels in ageing, Alzheimer's, and small vessel disease. *Brain*. 2019;142(4):1093-1107. doi:10.1093/brain/awz026
46. Daianu M, Jahanshad N, Nir TM, et al. Rich club analysis in the Alzheimer's disease connectome reveals a relatively undisturbed structural core network. *Hum Brain Mapp*. 2015;36(8):3087-3103. doi:10.1002/hbm.22830
47. Wang Y, Yang D, Li Q, Kaufer D, Styner M, Wu G. Characterizing the Propagation Pattern of Neurodegeneration in Alzheimer's Disease by Longitudinal Network Analysis. In: *2020 IEEE 17th International Symposium on Biomedical Imaging (ISBI)*. ; 2020:292-295. doi:10.1109/ISBI45749.2020.9098513
48. Convit A, de Asis J, de Leon MJ, Tarshish CY, De Santi S, Rusinek H. Atrophy of the medial occipitotemporal, inferior, and middle temporal gyri in non-demented elderly predict decline to Alzheimer's disease☆. *Neurobiol Aging*. 2000;21(1):19-26. doi:10.1016/S0197-4580(99)00107-4
49. Scheff SW, Price DA, Schmitt FA, Scheff MA, Mufson EJ. Synaptic Loss in the Inferior Temporal Gyrus in Mild Cognitive Impairment and Alzheimer's Disease. *J Alzheimers Dis*. 2011;24(3):547-557. doi:10.3233/JAlzheimer's disease-2011-101782
50. Arenaza-Urquijo EM, Vemuri P. Resistance vs resilience to Alzheimer disease: Clarifying terminology for preclinical studies. *Neurology*. 2018;90(15):695-703. doi:10.1212/WNL.0000000000005303
51. Cai H, Cong W, Ji S, Rothman S, Maudsley S, Martin B. Metabolic Dysfunction in Alzheimer's Disease and Related Neurodegenerative Disorders. *Curr Alzheimer Res*. 2012;9(1):5-17. doi:10.2174/156720512799015064
52. Fornari S, Schäfer A, Jucker M, Goriely A, Kuhl E. Prion-like spreading of Alzheimer's disease within the brain's connectome. *J R Soc Interface*. 2019;16(159):20190356. doi:10.1098/rsif.2019.0356
53. Kaufman SK, Sanders DW, Thomas TL, et al. Tau Prion Strains Dictate Patterns of Cell Pathology, Progression Rate, and Regional Vulnerability In Vivo. *Neuron*. 2016;92(4):796-812. doi:10.1016/j.neuron.2016.09.055
54. Braak H, Braak E. Neuropathological staging of Alzheimer-related changes. *Acta Neuropathol (Berl)*. 1991;82(4):239-259. doi:10.1007/BF00308809
55. Zhang J, Yang D, He W, Wu G, Chen M. A Network-Guided Reaction-Diffusion Model of AT[N] Biomarkers in Alzheimer's Disease. In: *2020 IEEE 20th International Conference on Bioinformatics and Bioengineering (BIBE)*. ; 2020:222-229. doi:10.1109/BIBE50027.2020.00044
56. Fagan AM, Xiong C, Jasielec MS, et al. Longitudinal Change in CSF Biomarkers in Autosomal-Dominant Alzheimer's Disease. *Sci Transl Med*. 2014;6(226):226ra30-226ra30. doi:10.1126/scitranslmed.3007901

57. Luo J, Wärmländer SKTS, Gräslund A, Abrahams JP. Cross-interactions between the Alzheimer Disease Amyloid- β Peptide and Other Amyloid Proteins: A Further Aspect of the Amyloid Cascade Hypothesis. *J Biol Chem.* 2016;291(32):16485-16493. doi:10.1074/jbc.R116.714576
58. Xin S-H, Tan L, Cao X, Yu J-T, Tan L. Clearance of Amyloid Beta and Tau in Alzheimer's Disease: from Mechanisms to Therapy. *Neurotox Res.* 2018;34(3):733-748. doi:10.1007/s12640-018-9895-1
59. Zlokovic BV, Yamada S, Holtzman D, Ghiso J, Frangione B. Clearance of amyloid β -peptide from brain: transport or metabolism? *Nat Med.* 2000;6(7):718-718. doi:10.1038/77397
60. Menkes-Caspi N, Yamin HG, Kellner V, Spires-Jones TL, Cohen D, Stern EA. Pathological Tau Disrupts Ongoing Network Activity. *Neuron.* 2015;85(5):959-966. doi:10.1016/j.neuron.2015.01.025
61. Palop JJ, Chin J, Mucke L. A network dysfunction perspective on neurodegenerative diseases. *Nature.* 2006;443(7113):768-773. doi:10.1038/nature05289